

## Assaad Alsahlani

Department of Mechanical and Civil Engineering,  
Purdue University Northwest,  
Hammond, IN 46323  
e-mail: aabbassa@pnw.edu

## Kelvin Randhir

Department of Mechanical Engineering,  
Michigan State University,  
East Lansing, MI 48823  
e-mail: randhirk@msu.edu

## Michael Hayes

Department of Mechanical Engineering,  
Michigan State University,  
East Lansing, MI 48823  
e-mail: hayesm33@msu.edu

## Philipp Schimmels

Department of Mechanical Engineering,  
Michigan State University,  
East Lansing, MI 48823  
e-mail: schimm16@msu.edu

## Nesrin Ozalp<sup>1</sup>

Fellow ASME

Department of Mechanical and Civil Engineering,  
Purdue University Northwest,  
Hammond, IN 46323  
e-mail: nozalp@pnw.edu

## James Klausner

Fellow ASME

Department of Mechanical Engineering,  
Michigan State University,  
East Lansing, MI 48823  
e-mail: jklausner@fraunhofer.org

# Design of a Combined Proportional Integral Derivative Controller to Regulate the Temperature Inside a High-Temperature Tubular Solar Reactor

*Solar fuels are proven to be promising candidates for thermochemical energy storage. However, the transient nature of solar radiation is an obstacle to maintaining a stable operational temperature inside a solar reactor. To overcome this challenge, the temperature of a solar reactor can be regulated by controlling the incoming solar radiation or the feedstock flowrate inside the reactor. In this work, a combined proportional integral derivative (PID) controller is implemented to regulate the temperature inside a high-temperature tubular solar reactor with counter-current flowing gas/particles. The control model incorporates two control systems to regulate incoming solar radiation and gas flow simultaneously. The design of the controller is based on a reduced-order numerical model of a high-temperature tubular solar reactor that is vertically oriented with an upward gas flow and downward particle flow. The reactor receives heat circumferentially through its wall over a finite segment of its length. Formulation of the heat transfer model is presented by applying the energy balance for the reactor tube and considering heat and mass transfer inside. A set of governing differential equations are solved numerically by using the finite volume method to obtain reactor wall, particles, and gas temperatures along the reactor length with various boundary conditions. Simulation results are used to tune the PID controller parameters by utilizing the Ziegler–Nichols tuning method. Both the simulation results and the controller performance are visualized on the LABVIEW platform. The controller is challenged to track different temperature setpoints with different scenarios of transient solar radiation. The performance of the PID controller was compared to experimental results obtained from an industrial PID controller embedded in a 7 kW electric furnace. Results show that the combined PID controller is successful in maintaining a stable temperature inside the reactor by regulating the incoming solar radiation and the flowrate via small steady-state error and reasonable settling time and overshoot. [DOI: 10.1115/1.4055296]*

**Keywords:** solar reactor, solar fuel, temperature control, PID controller, heat transfer

## 1 Introduction

Solar fuels are produced by housing reactants within a solar reactor and the concentrated solar energy is transferred to the reactants through a window or indirectly transferred using a windowless reactor. Storing solar energy as pelletized solid state thermochemically reduced media for a long duration is a promising technology to produce solar fuel as a substitute for fossil fuels. However, the effectiveness of thermochemical energy storage systems is assessed based on a number of characteristics, such as the number of life cycles with respect to reusability, the duration of stable energy storage, and the volumetric heat capacity or energy density [1,2]. Furthermore, the production of high-temperature solar fuel requires an efficient solar receiver that utilizes solar energy as a heat source to activate endothermic processes where the solar fuel absorbs energy during the chemical conversion of reactants. The energy

stored in solar fuel can be released via an exothermic process when needed.

Thermochemical redox materials are considered as solar fuels, however, each type has a critical reduction temperature where the fuel charges and discharges energy. For instance, at relatively low temperatures of 250–800 °C, dehydration of metal hydroxides charges and discharges energy [3] whereas calcium hydride reacts in a temperature range of 1100–1400 °C [4]. On the other hand, BaO<sub>2</sub>/BaO have appreciable potential with their 20 useable lifetime cycles and critical reaction temperature in the range of 600–750 °C [5]. Similarly, cobalt oxide (Co<sub>3</sub>O<sub>4</sub>) and Co<sub>3</sub>O<sub>4</sub>/Al<sub>2</sub>O<sub>3</sub> react at temperature ranges of 840–940 °C [6] and 700–1000 °C [7]. For higher temperatures, magnesium manganese oxide (MgMn<sub>2</sub>O<sub>4</sub>) reacts between 1000 and 1500 °C and has been proven to show unique thermal characteristics and stability when stored at room temperature [8].

In high-temperature thermochemical reactions, a windowless plug-flow tubular solar reactor is preferable due to the melting limit of reactor components. Thermochemical conversion processes in reduction/oxidation require flowing gas to facilitate energy charging and discharging. Co-current flowing gas/media are commonly used in plug-flow tubular solar reactors; however, utilizing counter-current flowing gas can recuperate the sensible heat

<sup>1</sup>Corresponding author.

Contributed by the Solar Energy Division of ASME for publication in the JOURNAL OF SOLAR ENERGY ENGINEERING: INCLUDING WIND ENERGY AND BUILDING ENERGY CONSERVATION. Manuscript received April 26, 2022; final manuscript received August 10, 2022; published online September 26, 2022. Editor: S. A. Sherif.

which yields an energy-efficient process. The thermal performance of different solar receiver concepts can be tested experimentally. Nevertheless, numerical examination of thermal characteristics of a solar receiver or a reactor needs a rigorous analysis addressing different parameters\geometry in addition to the nature of the thermochemical process. Window-type solar receivers are usually used for fixed-bed reactors where the concentrated solar power irradiates the reactant through a quartz transparent window [9–11] or another type of indirectly irradiated cavity receivers [12]. Such solar receivers are numerically analyzed by implementing the Monte Carlo ray tracing method coupled with a heat transfer numerical model [9,10] or modeled in a three-dimensional computational domain using commercial software such as FLUENT package [13] or CFMESH [14].

On the other hand, indirectly heated fixed beds are numerically analyzed using the finite volume method whereas moving beds in tubular solar reactors are usually modeled as tubes subjected to external heat flux. Such an approach has been demonstrated in Refs. [15,16] by incorporating more complex parameters [17] since the thermal analysis considered was based on the heat transfer interaction between granular flows [18]. Recently, Huang et al. [19] developed a CFD model to analyze the thermal characteristics of a 1D model for thermochemical reactors with counter-current flowing media. The work was extended to analyze the same system with a 2D numerical model and reported an enhancement in the accuracy when compared to results obtained from the 1D model [20]. In general, simulating two-phase flow problems requires a meticulous CFD approach to achieve the desired level of accuracy.

The performance of solar applications including the efficiency of solar thermochemical processes depends on the stability of solar reactor temperature. To maintain a quasi-steady temperature within the reactor during on-sun operation, an efficient control system needs to be implemented. For example, controlling the heliostats via a feedback control system can adjust the direct normal irradiance (DNI) [21] which in return can regulate the reactor temperature. One of the key tools in regulating solar reactor temperature is the implementation of a proportional integral derivative (PID) controller as seen in Ref. [22] where the temperature of a tubular reactor is controlled. The PID controller with model-based feedforward control can be effectively implemented in solar direct steam generation (DSG) [23]. A simplified proportional integral (PI) controller is also a successful method to control the temperature inside a fixed-bed tubular reactor [24]. Manipulating the gas flow is another approach to regulate the temperature in steam gasification of Petcoke and carbothermal reduction [22]. For systems with high nonlinearity such as thermochemical reaction kinetics more advanced control methodology such as model predictive control (MPC) strategy is preferable since the process of solar fuel production is a complicated nonlinear process, and it involves multivariables such as gas flow, solar fuel mass flowrate, and solar flux [10,19]. Although the MPC controller is proven as an effective strategy in regulating the temperature of solar reactors [17,18] it requires more computational effort and optimization process in comparison to linear conventional PID controller.

This work presents a combined PID controller that is implemented in regulating the temperature inside a vertical tubular solar reactor with indirect heating. The solar reactor is used to produce solar fuel by flowing ( $\text{MgMn}_2\text{O}_4$ ) particles downward and counter-current gas flowing upward to charge and discharge the solar fuel. The control system utilizes heat flux and particles\gas flow as input variables to maintain a constant temperature inside the solar reactor. A low-order physical model was developed to simulate the thermal characteristics of the tubular solar reactor and the simulation results were used to tune the PID controller.

## 2 Methodology

Concentrated solar power is utilized as thermal energy provided to the system by heating a segment of the reactor tube defined as the heating zone. The reactants pellets are fed from the top and they

flow downward through the reactor tube, reaching the required reaction temperature at the heating zone where the thermochemical reaction occurs. The gas is supplied to the reactor tube from the bottom which flows upward. The counter-current gas flow offers a more efficient operation because the oxidized porous pellets are preheated by the hot interstitial gas flowing upward, which passes through the heated zone as shown in Fig. 1. To ensure an efficient recuperation, the sensible heat, the amounts of gas, and particle mass flowrates should be adjusted accordingly. In the following sections, the reactor system will be modeled numerically to develop a low-order physical model and the proposed model will be used to design the control system.

**2.1 Low-Order Numerical Modeling.** The reactor assembly shown in Fig. 1 was analyzed numerically by modeling the heat transferred by conduction, convection, and radiation between the reactor tube and interpenetrating solid/gas phases. The tube model is subjected to a constant heat flux over a portion of its length and the center of the heating zone is located at the midpoint of the tube length as illustrated in Fig. 2. The reactor tube and its interior were discretized into a number of finite control volumes, and the model was developed based on the assumption that superficial gas velocity remains constant along the flow path. The formulation of the temperature profiles was derived in our previous work for a horizontal reactor [24] which is used as a foundation for a vertical solar reactor:

— Energy balance of the reactor wall

$$\rho_w c_{pw} \frac{\partial T_w}{\partial t} = \frac{\partial}{\partial x} \left( k_w \frac{\partial T_w}{\partial x} \right) + h_{gw} a_w (T_g - T_w) + h_{sw} a_w (T_s - T_w) + h_r a_w (T_s - T_w) + h_{\infty} a_w (T_{\infty} - T_w) + a_{wo} q_s'' \quad (1)$$

— Energy balance of the gas

$$\varepsilon \rho_g c_{pg} \frac{\partial T_g}{\partial t} + \rho_g c_{pg} \mathbf{u}_g \frac{\partial T_g}{\partial x} = \frac{\partial}{\partial x} \left( k_g^{ef} \frac{\partial T_g}{\partial x} \right) + h_{gs} a_{gs} (T_s - T_g) + h_{gw} a_w (T_w - T_g) \quad (2)$$

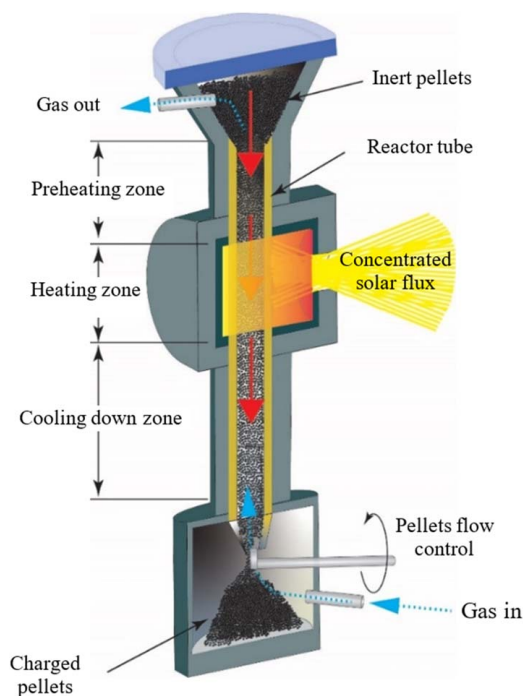


**Fig. 1 Cross-sectional view of the reactor with particles and gas flows**

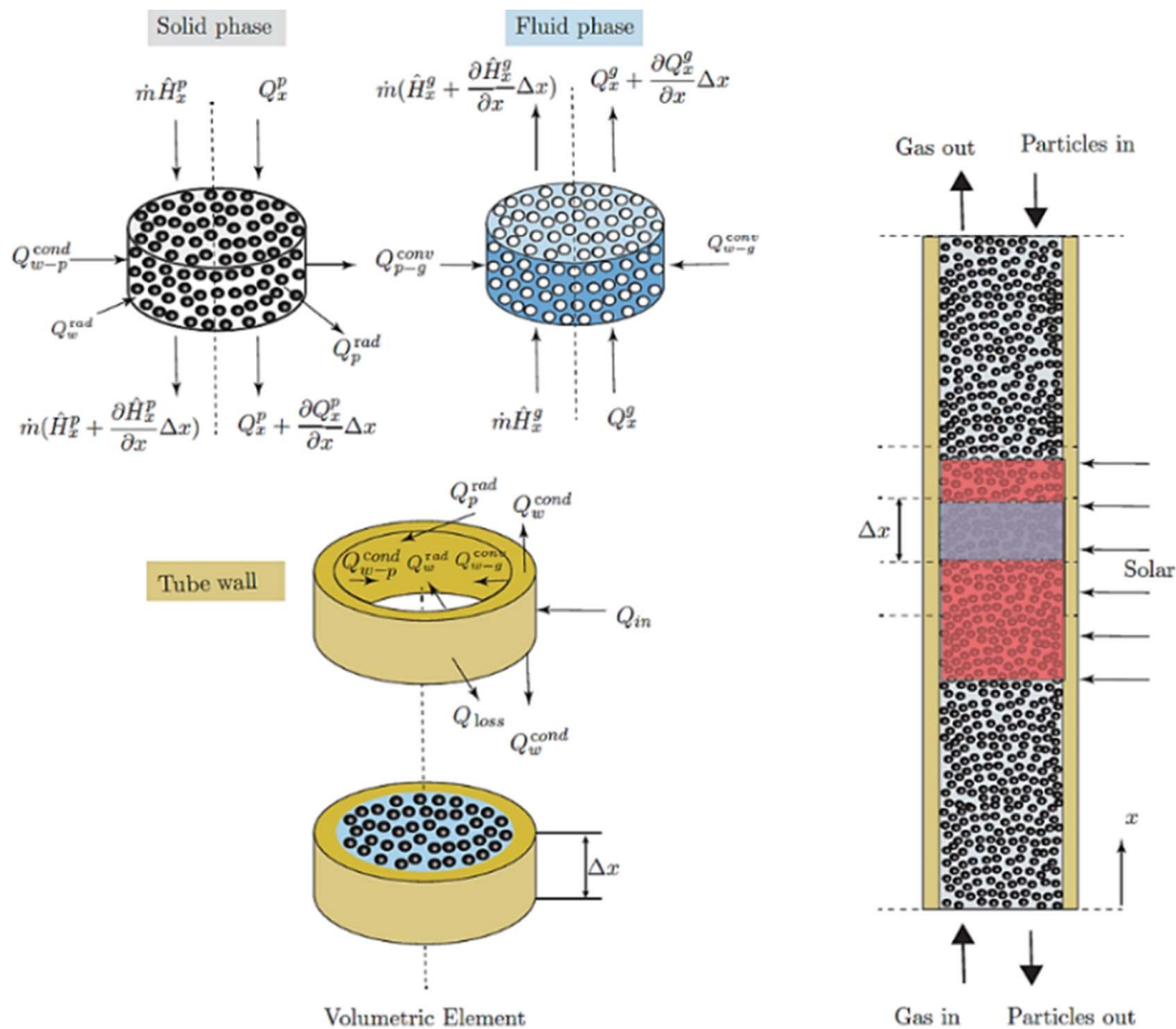


Fig. 2 Schematic of the heat transfer model of vertical reactor tube and solar fuel particles

— Energy balance of the particles

$$(1 - \varepsilon) \rho_s c_{p_s} \frac{\partial T_s}{\partial t} + \rho_s c_{p_s} \mathbf{v}_s \frac{\partial T_s}{\partial x} = \frac{\partial}{\partial x} \left( k_s^{ef} \frac{\partial T_s}{\partial x} \right) + h_{gs} a_{gs} (T_g - T_s) + h_{sw} a_w (T_w - T_s) + h_r a_w (T_w - T_s) + S_R \quad (3)$$

where  $s$ ,  $g$ , and  $w$  stand for the solar fuel, gas, and tube wall, respectively.  $\mathbf{u}_g$  and  $\mathbf{v}_s$  are the gas and particles flow velocities, respectively.  $\rho$  is the mass density,  $c_p$  is the specific heat capacity, and  $\varepsilon$  is the porosity.  $S_R$  stands for the heat absorbed by reaction kinetics. The boundary conditions for the particles and gas inlet/outlet temperatures are

$$\text{At } x = 0, \quad T_g = (T_g)_{in} \quad \text{and} \quad \frac{\partial T_s}{\partial x} = 0 \quad (4)$$

$$\text{At } x = L, \quad T_s = (T_s)_{in} \quad \text{and} \quad \frac{\partial T_g}{\partial x} = 0 \quad (5)$$

The differential equations of the heat transfer model described in Eqs. (1)–(3) are discretized into 100 cylindrical-shaped control volumes as illustrated in Fig. 2. The diffusion term was discretized

using second-order central differencing, third-order upwind scheme (QUICK) for convection, and Crank–Nicolson method in time.

**2.2 Validation of the Numerical Model.** To validate the accuracy of the model described in Eqs. (1)–(3), an experimental test was performed. The experimental setup consists of a 121.92 cm in length alumina tube centered vertically through a 30.5 cm heating zone as shown in Fig. 3. The tubular reactor is surrounded by heating elements controlled by a 7 kW electric tube furnace. A funnel filled with  $\text{MgMn}_2\text{O}_4$  particles is mounted at the top of the reactor and it receives  $3.66 \pm 0.516$  mm  $\text{MgMn}_2\text{O}_4$  particles from the funnel. The mass flowrate of the particles is controlled by a gas-pulsation valve mechanism at the bottom end of the tubular reactor and the discharged particles are collected within a tank beneath the setup. A counter-current flowing gas (air) is supplied to the tubular reactor from the bottom end and the gas flowrate is controlled by a digital Alicat gas flow controller. Six B-type thermocouples are mounted on the outside of the reactor tube to record temperature as shown in Fig. 3, and the measured data are recorded by a GraphTec digital data logger.

During the experimental testing, the reactor tube was filled with a packed bed and heated up from room temperature to 1000 °C, then maintained at constant temperature for 30 min. As the next step, particle/gas flow was initiated (particles mass flowrate = 1 g/s and gas flowrate = 40 SLPM) as the system was heating up to

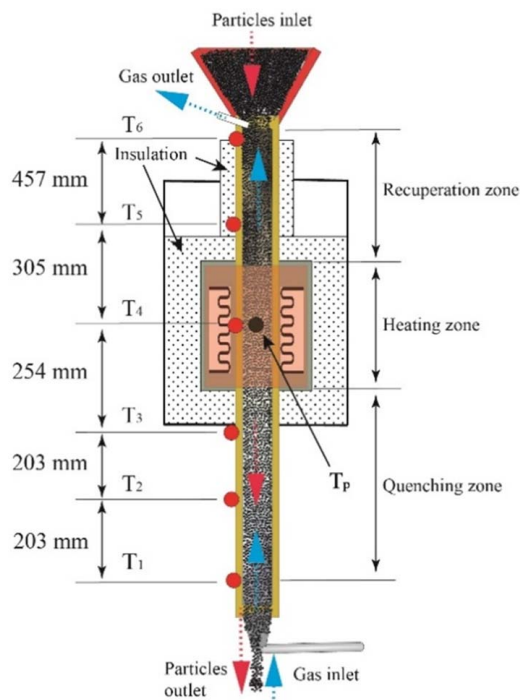


**Fig. 3 Schematic diagram of the experimental setup**

1400 °C. The in-house code was tested by simulating the conditions described in the experimental run by using the parameters and correlations listed in Table 1, and the thermal properties and dimensions listed in Table 2. Figure 4 illustrates the numerical and experimental results of the temperature distribution along the reactor tube at 1000 °C and 1400 °C. As it is seen, the low-order numerical model exhibited a good agreement between the experimental and numerical results.

### 3 Design of the Control System

The control system consists of two controllers; the first controller is to regulate the input heat flux, whereas the second controller adjusts the particles mass flowrate as shown in Fig. 5. To maintain the heat recuperation condition, mass flowrates of the gas and particles are interrelated which technically required one controller.

For the input heat flux, a conventional PID controller is implemented since it is the most commonly used control method in the industry. The control action  $\Delta u$  is defined by the discrete-time form of the PID controller as follows:

$$\Delta u(t_k) = \left( K_P + \frac{K_P \Delta t}{\tau_I} + \frac{K_P \tau_D}{\Delta t} \right) e(t_k) - \left( K_P + \frac{2K_P \tau_D}{\Delta t} \right) e(t_{k-1}) + \frac{K_P \tau_D}{\Delta t} e(t_{k-2}) \quad (6)$$

where  $K_P$ ,  $\tau_D$ , and  $\tau_I$  are the controller parameters to be tuned using the Ziegler–Nichols method.  $e(t_k)$  is the error between the desired output and its setpoint at sampling time  $t_k$ , and  $\Delta t$  is the sampling time interval. On the other hand, the particle mass flowrate is controlled by implementing a controller that adjusts the amount of particles/gas flowrate when needed. The flow controller is an incremental controller with a fixed value of mass flow increment and the flow controller is to be activated when the heat flux controller is saturated or failed to track the desired setpoint because of insufficient input power. The simulation of the low-order model and the controllers were visualized by displaying the results using LABVIEW. The amounts of particles/gas mass flowrates and input power can be adjusted manually from the display window when the system is switched to open-loop mode.

### 4 Results and Discussions

The performance of the control system was simulated by using the thermal properties, dimensions, parameters, and correlations listed in Tables 1 and 2. The input flux PID controller is tuned by using the Ziegler–Nichols method [32] where the controller parameters were tuned to the values of  $K_P = 10$ ,  $\tau_I = 262.8$ , and  $\tau_D = 0.0001$ . The controller was tested to track ramping setpoint where the system was heated from room temperature to a constant temperature of 1400 °C. The test included three values of particles/gas mass flowrates as shown in Fig. 5 and the simulation results were compared with experimental results obtained from a 7 kW electric furnace equipped with a conventional PID controller.

The 7 kW was used to heat the system up to 1400 °C following different ramping patterns as shown in Fig. 6. Three experimental tests were used with different amounts of particles/gas mass flowrate for each run. The same operation conditions were used to simulate the performance of the flux PID controller. As seen in Fig. 6, the simulation results showed good tracking performance for the proposed PID controller and a reasonable agreement in the input power. For all cases, the steady-state error is zero and the maximum overshoot is 2% for the simulation results. However, the industrial PID controller showed better performance with

**Table 1 List of parameters and correlations**

Parameter	Symbol	Value/correlation	Ref.
Porosity	$\varepsilon$	$0.375 + 0.34 \frac{d_p}{D_i}$	[25]
Solid–gas heat transfer coefficient	$h_{sg}$	$\left( 2 + 1.2 R_e^{1/2} \cdot P_r^{1/3} \right) \frac{k_g}{d_p}$	[26]
Solid-wall heat transfer coefficient	$h_{sw}$	$\frac{1}{0.085 + \frac{1}{2} \sqrt{\frac{\pi}{P_{eL}}} \frac{k_g}{d_p}}$	[27]
Wall-gas heat transfer coefficient	$h_{wg}$	$(0.023 R_e^{0.8} \cdot P_r^{0.4}) \frac{k_g}{D_i}$	[28]
Radiation heat transfer coefficient	$h_r$	$\frac{\sigma(T_s^2 + T_w^2)(T_s + T_w)}{\frac{1}{e_b} + \frac{1}{e_w} - 1}$	Derived from [28]
Emissivity of the bulk	$e_b$	0.5(1 + $e_p$ )	[28]
Emissivity of the tube wall	$e_w$	0.7	[29]
Emissivity of the particles	$e_p$	0.7	



Table 2 List of thermal properties and dimensions

Material	Thermal conductivity (W/m K)	Specific heat (J/kg K)	Mass density (kg/m <sup>3</sup> )	Dimensions (mm)
Reactor tube (alumina)	$k_w = -1.495 \times 10^{-13} T_w^5 + 4.123 \times 10^{-10} T_w^4 - 4.47 \times 10^{-7} T_w^3 + 2.69 \times 10^{-4} T_w^2 - 0.117 T_w + 34.96$ [30]	$Cp_w = 2.696 \times 10^{-16} T_w^5 - 1.69 \times 10^{-12} T_w^4 + 3.933 \times 10^{-9} T_w^3 - 4.267 \times 10^{-6} T_w^2 + 2.3 \times 10^{-3} T_w + 0.691$ [30]	3900	$D_o = 57.15$ , $D_i = 50.8$
Insulation	0.315	—	—	Thickness: 14.7
Gas (air-averaged)	0.0873	1206	0.88	—
Particles (MgMn <sub>2</sub> O <sub>4</sub> )	$k_s = 5.27 \times 10^{-10} T_s^3 - 1.89 \times 10^{-7} T_s^2 + 4.72 \times 10^{-4} T_s + 0.3889$ [31]	870	$(1 - \epsilon) \rho_s = 2003$	Size = 3.66

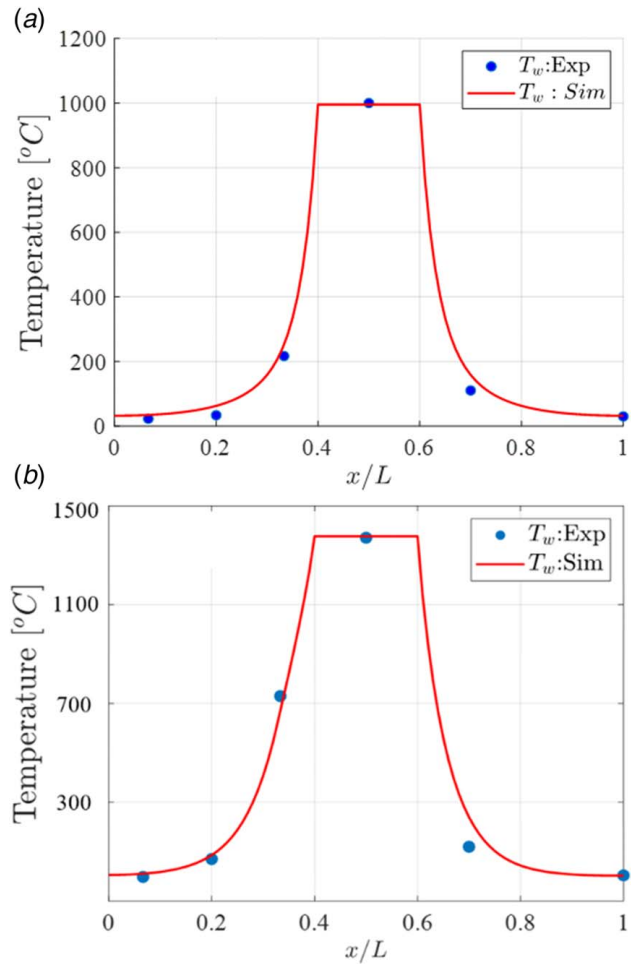


Fig. 4 Comparison between experimental and numerical results at (a) 1000 °C and (b) 1400 °C

smaller overshoot when the setpoint was changed from ramping up to constant steady-state temperature.

The code was deployed on a LABVIEW model to visualize the simulation performance of the controller with different scenarios. Control of the particle mass flowrate is implemented to change the particle mass flowrate by 0.1 g/s and the mass flowrate limits were constrained to  $2.5 \text{ g/s} \geq \dot{m}_s \geq 0 \text{ g/s}$  and the controller initiates the desired particle flowrate when the reactor temperature reaches 1000 °C. The controller performance and robustness were tested through three scenarios during the operation of the solar reactor. First, the system was heated up from room temperature to 1400 °C with a heating rate of 5 °C/min and preserved constantly for 60 min as shown in Fig. 7 where the particles mass flowrate is fixed to 0.75 g/s.

To simulate the performance of the mass flowrate controller, the input power was fixed constant at 2.26 kW to simulate an excessive input power scenario. As the input power increased, the reactor temperature increased and the flow controller started increasing the particle mass flowrate to cool down the reactor and bring the temperature back to the setpoint. The third scenario simulated a partially cloudy weather where the input power was fixed to 1.76 kW. As seen in Fig. 7, the temperature decreased rapidly and the flow controller started decreasing the particle mass flowrate in order to increase the temperature inside the reactor. In all scenarios, the PID controller tracked the desired setpoint successfully by manipulating input heat flux and particles mass flowrate. The steady-state error is almost eliminated and the maximum overshoot was not exceeding 1% for both heat flux and mass flowrate controllers.

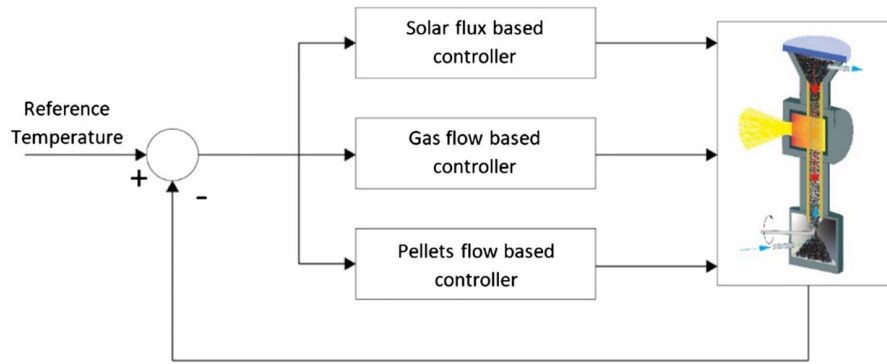


Fig. 5 Control system loop to regulate reactor temperature at the heating zone

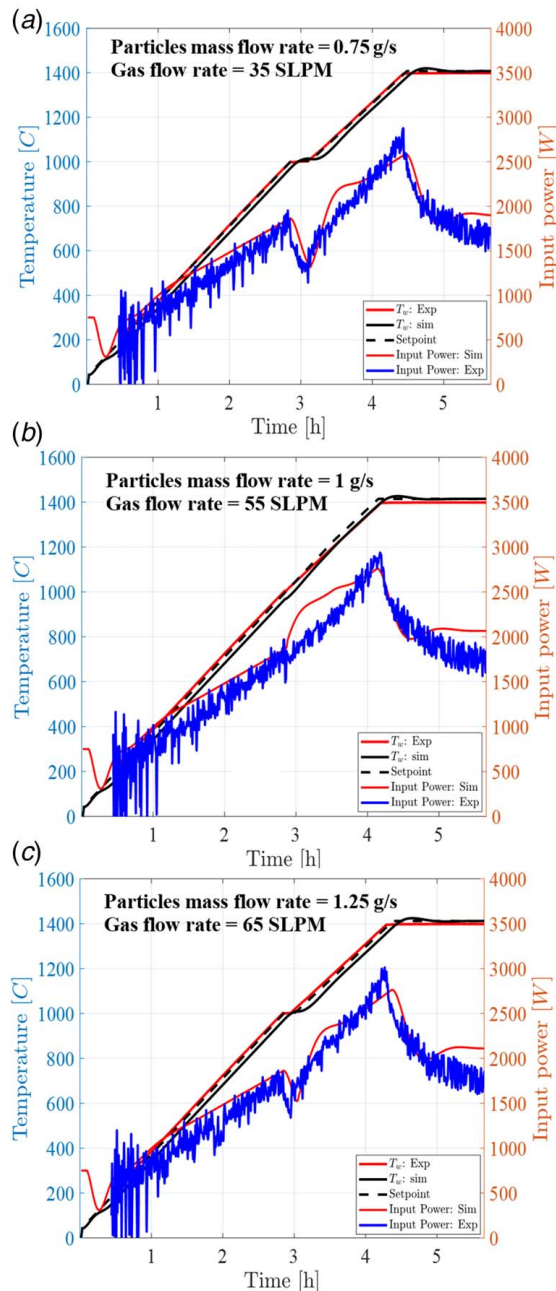


Fig. 6 Numerical and experimental results of tracking setpoints for different gas/particles mass flowrates: (a) 0.75 g/s, (b) 1 g/s, and (c) 1.25 g/s

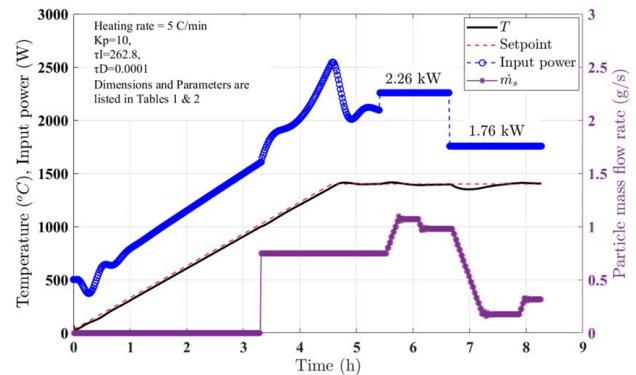


Fig. 7 Performance of the flow controller: simulation results

It should be noted that the flow controller manipulates the particle mass flowrate which is interrelated to the corresponding gas flowrate (which is air in this work). The amount of required gas flowrate was calculated by  $(C_p \dot{m})_{air} = (C_p \dot{m})_{particles}$  where the sensible heat is recuperated within the heating zone and the inlet and outlet temperature of gas/particles are maintained approximately at room temperature. Practically, the particles mass flowrate can be controlled by using an L-valve pulsation mechanism which is proportional to the amount of required gas flowrate provided by a digital Alicat gas flow controller. On the other hand, the incoming input power received from solar irradiance can be adjusted via variable aperture size mechanism [9] or by utilizing the heliostat aiming method [33].

More advanced control methodologies are such as MPC [9] or implementing nonlinear control theory [34].

## 5 Conclusions

A combined (PID) controller was designed to regulate the temperature inside a high-temperature tubular solar reactor. The reactor system consists of a vertical tube surrounded by heating elements over a portion of its length. The reactant particles flow downward through the tube and counter-current flowing gas was supplied from the bottom of the tube. A low-order physical model was developed to simulate the thermal performance of the solar reactor during the operation. The numerical formulation of the heat transfer model was presented by applying the energy balance for the reactor tube and the interior considering heat and mass transfer. The control system consists of two controllers to regulate the incoming solar radiation and the gas flow simultaneously as needed. It should be noted that the gas flowrate is interrelated to the particle mass flowrate as the heat recuperation condition is maintained. Hence, changing particle mass flowrate will change the gas flowrate

spontaneously. The in-house code was validated by simulating an experimental test with a particle mass flowrate of 1 g/s and a gas flowrate of 40 SLPM. The experimental and simulation results of temperature distribution along the reactor tube were compared at two temperatures; namely, 1000 °C and 1400 °C, where the proposed physical model showed good agreement. Simulation results were used to tune the PID controller using the Ziegler–Nichols method with tuned parameters of  $K_P=10$ ,  $\tau_I=262.8$ , and  $\tau_D=0.0001$ . Simulation results of the in-house code and PID controller were tested with different particles/gas mass flowrates and the simulation was visualized on the LABVIEW platform from (National Instruments) to simulate different operation conditions by challenging the control system with different values of transient solar power. First, the system was tested to track a ramping setpoint with a 5 °C/min heating rate where the controller heated the reactor from room temperature to 1400 °C as the final constant setpoint. At steady-state temperature, the controller was tested via two different scenarios. The transient nature of the solar power was simulated by limiting the input power to 2.25 kW in the second scenario and limiting the input power to 1.75 kW in the third scenario. In all scenarios, the control system manipulated the incoming solar radiation and particle mass flow accordingly within the operating limits and maintained a small overshoot and reasonable settling time when incoming solar radiation is sufficient. In general, the steady-state error is almost eliminated and the maximum overshoot was not exceeding 1% for both heat flux and mass flowrate controllers. The current model is simple and fast and can be used effectively in high-temperature solar applications with thermochemical reactions.

## Acknowledgment

This material is based upon work supported by the U.S. Department of Energy's Office of Energy Efficiency and Renewable Energy (EERE) under the Solar Energy Technology Office (SETO) Award Number DE-EE0008992.

## Conflict of Interest

There are no conflicts of interest.

## Data Availability Statement

The authors attest that all data for this study are included in the paper.

## Nomenclature

$a_{gs}$  = gas-particles area per volume ( $\text{m}^{-1}$ )  
 $a_w$  = particles-wall area per volume ( $\text{m}^{-1}$ )  
 $c_p$  = specific heat ( $\text{J kg}^{-1} \text{K}^{-1}$ )  
 $e_b$  = emissivity of the bulk  
 $e_p$  = emissivity of the SoFuel particles  
 $e_w$  = emissivity of the tube wall  
 $h_{gs}$  = solid-to-gas convective heat transfer coefficient ( $\text{W m}^{-2} \text{K}^{-1}$ )  
 $h_{gw}$  = gas-to-wall convective heat transfer coefficient ( $\text{W m}^{-2} \text{K}^{-1}$ )  
 $h_r$  = radiation heat transfer coefficient ( $\text{W m}^{-2} \text{K}^{-1}$ )  
 $h_{sw}$  = solid-to-wall convective heat transfer coefficient ( $\text{W m}^{-2} \text{K}^{-1}$ )  
 $h_\infty$  = convection transfer coefficient ( $\text{W m}^{-2} \text{K}^{-1}$ )  
 $k_{ef}^g$  = effective thermal conductivity of gas ( $\text{W m}^{-2} \text{K}^{-1}$ )  
 $k_{ef}^s$  = effective thermal conductivity of pellets ( $\text{W m}^{-2} \text{K}^{-1}$ )  
 $q''$  = heat flux ( $\text{W m}^{-2}$ )  
 $t_r$  = particles residence time (s)  
 $D_i$  = tube inner diameter (m)  
 $D_o$  = tube outside diameter (m)  
 $K_p$  = proportional coefficient of PID controller

Pe = Péclet number  
 Pr = Prandtl number  
 $Q_{in}$  = input power at heating zone (W)  
 Re = Reynolds number  
 $T_g$  = gas temperature (K)  
 $T_s$  = solar fuel temperature (K)  
 $T_w$  = reactor wall temperature (K)  
 $T_\infty$  = ambient temperature (K)  
 $u_g, v_s$  = gas and particles velocities ( $\text{m s}^{-1}$ )

## Greek Symbols

$\varepsilon$  = porosity  
 $\rho$  = mass density ( $\text{kg m}^{-3}$ )  
 $\tau_D$  = derivative coefficient of PID controller  
 $\tau_I$  = integral coefficient of PID controller

## References

- [1] Farulla, G., Cellura, M., Guarino, F., and Ferraro, M., 2020, "A Review of Thermochemical Energy Storage Systems for Power Grid Support," *Appl. Sci.*, **10**(9), p. 3142.
- [2] Enescu, D., Chicco, G., Porumb, R., and Seritan, G., 2020, "Thermal Energy Storage for Grid Applications: Current Status and Emerging Trends," *Energies*, **13**(2), p. 340.
- [3] Prieto, C., Cooper, P., Fernández, A. I., and Cabeza, L. F., 2016, "Review of Technology: Thermochemical Energy Storage for Concentrated Solar Power Plants," *Renewable Sustainable Energy Rev.*, **60**, pp. 909–929.
- [4] Rönnebro, E. C. E., Whyatt, G., Powell, M., Westman, M., Zheng, F., and Fang, Z. Z., 2015, "Metal Hydrides for High-Temperature Power Generation," *Energies*, **8**(8), pp. 8406–8430.
- [5] Bayon, A., Bader, R., Jafarian, M., Fedunik-Hofman, L., Sun, Y., Hinkley, J., Miller, S., and Lipiński, W., 2018, "Techno-Economic Assessment of Solid-Gas Thermochemical Energy Storage Systems for Solar Thermal Power Applications," *Energy*, **149**, pp. 473–484.
- [6] Hutchings, K. N., Wilson, M., Larsen, P. A., and Cutler, R. A., 2006, "Kinetic and Thermodynamic Considerations for Oxygen Absorption/Desorption Using Cobalt Oxide," *Solid State Ionics*, **177**(1–2), pp. 45–51.
- [7] Karagiannakis, G., Pagkoura, C., Halevas, E., Baltzopoulou, P., and Konstandopoulos, A. G., 2016, "Cobalt/Cobaltous Oxide Based Honeycombs for Thermochemical Heat Storage in Future Concentrated Solar Power Installations: Multi-Cyclic Assessment and Semi-quantitative Heat Effects Estimations," *Sol. Energy*, **133**, pp. 394–407.
- [8] Randhir, K., King, K., Rhodes, N., Li, L., Hahn, D., Mei, R., AuYeung, N., and Klausner, J., 2019, "Magnesium–Manganese Oxides for High Temperature Thermochemical Energy Storage," *J. Energy Storage*, **21**, pp. 599–610.
- [9] Abedini Najafabadi, H., and Ozalp, N., 2018, "Aperture Size Adjustment Using Model Based Adaptive Control Strategy to Regulate Temperature in a Solar Receiver," *Sol. Energy*, **159**, pp. 20–36.
- [10] Zoller, S., Koepf, E., Roos, P., and Steinfeld, A., 2019, "Heat Transfer Model of a 50 kW Solar Receiver–Reactor for Thermochemical Redox Cycling Using Cerium Dioxide," *ASME J. Sol. Energy Eng.*, **141**(2), p. 021014.
- [11] Lichty, P., Perkins, C., Woodruff, B., Bingham, C., and Weimer, A., 2010, "Rapid High Temperature Solar Thermal Biomass Gasification in a Prototype Cavity Reactor," *ASME J. Sol. Energy Eng.*, **132**(1), p. 011012.
- [12] Sedighi, M., Taylor, R. A., Lake, M., Rose, A., Izadgoshasb, I., and Vasquez Padilla, R., 2020, "Development of a Novel High-Temperature, Pressurised, Indirectly-Irradiated Cavity Receiver," *Energy Convers. Manage.*, **204**, p. 112175.
- [13] Li, X., Li, R., Chang, H., Zeng, L., Xi, Z., and Li, Y., May 2022, "Numerical Simulation of a Cavity Receiver Enhanced With Transparent Aerogel for Parabolic Dish Solar Power Generation," *Energy*, **246**, p. 123358.
- [14] Kuruneru, S. T. W., Kim, J. S., Soo Too, Y. C., and Potter, D., 2022, "Discrete Particle Modelling of Buoyant Convective Particle-Laden Air Flow in Solar Cavity Free-Falling Particle Receivers," *Energy Reports*, **8**, pp. 3902–3918.
- [15] Abedini Najafabadi, H., and Ozalp, N., 2018, "An Advanced Modeling and Experimental Study to Improve Temperature Uniformity of a Solar Receiver," *Energy*, **165**(Part B), pp. 984–998.
- [16] Wang, B., Li, L., Pottas, J. J., Bader, R., Kreider, P. B., Wheeler, V. M., and Lipiński, W., 2020, "Thermal Model of a Solar Thermochemical Reactor for Metal Oxide Reduction," *ASME J. Sol. Energy Eng.*, **142**(5), p. 051002.
- [17] Wytenbach, J., Bougard, J., Descy, G., Skrylnyk, O., Courbon, E., Frère, M., and Bruyat, F., 2018, "Performances and Modelling of a Circular Moving bed Thermochemical Reactor for Seasonal Storage," *Appl. Energy*, **230**, pp. 803–815.
- [18] Guo, Z., Yang, J., Tan, Z., Tian, X., and Wang, Q., 2021, "Numerical Study on Gravity-Driven Granular Flow Around Tube Out-Wall: Effect of Tube Inclination on the Heat Transfer," *Int. J. Heat Mass Transfer*, **174**, p. 121296.
- [19] Huang, W., Korba, D., Randhir, K., Petrasch, J., Klausner, J., AuYeung, N., and Li, L., 2022, "Thermochemical Reduction Modeling in a High-Temperature Moving-Bed Reactor for Energy Storage: 1D Model," *Appl. Energy*, **306**(Part B), p. 118009.

- [20] Korba, D., Huang, W., Randhir, K., Petrasch, J., Klausner, J., AuYeung, N., and Li, L., 2022, "A Continuum Model for Heat and Mass Transfer in Moving-Bed Reactors for Thermochemical Energy Storage," *Appl. Energy*, **313**, p. 118842.
- [21] Mészáros, A., Rusnák, A., and Fikar, M., 1999, "Adaptive Neural PID Control Case Study: Tubular Chemical Reactor," *Comput. Chem. Eng.*, **23**, pp. S847–S850.
- [22] Petrasch, J., Osch, P., and Steinfeld, A., 2009, "Dynamics and Control of Solar Thermochemical Reactors," *Chem. Eng. J.*, **145**(3), pp. 362–370.
- [23] Mokhtar, M., Zahler, C., and Stieglitz, R., 2022, "Control of Concentrated Solar Direct Steam Generation Collectors for Process Heat Applications," *ASME J. Sol. Energy Eng.*, **144**(1), p. 011005.
- [24] Al Sahlani, A., Randhir, K., Ozalp, N., and Klausner, J., 2022, "A Forward Feedback Control Scheme for a Solar Thermochemical Moving Bed Counter-Current Flow Reactor," *ASME J. Sol. Energy Eng.*, **144**(3), p. 031004.
- [25] Wen, D., and Ding, Y., 2006, "Heat Transfer of Gas Flow Through a Packed Bed," *Chem. Eng. Sci.*, **61**(11), pp. 3532–3542.
- [26] Yuen, M. C., and Chen, L. W., May 1978, "Heat-Transfer Measurements of Evaporating Liquid Droplets," *Int. J. Heat Mass Transfer*, **21**(5), pp. 537–542.
- [27] Sullivan, W. N., and Sabersky, R. H., 1975, "Heat Transfer to Flowing Granular Media," *Int. J. Heat Mass Transfer*, **18**(1), pp. 97–107.
- [28] Stenberg, V., Sköldberg, V., Öhrby, L., and Rydén, M., 2019, "Evaluation of Bed-to-Tube Surface Heat Transfer Coefficient for a Horizontal Tube in Bubbling Fluidized Bed at High Temperature," *Powder Technol.*, **352**, pp. 488–500.
- [29] Sih, S. S., and Barlow, J. W., 2004, "The Prediction of the Emissivity and Thermal Conductivity of Powder Beds," *Part. Sci. Technol.*, **22**(3), pp. 291–304.
- [30] Touloukian, Y. S., and Buyco, E. H., 1970, *Specific Heat: Nonmetallic Solids*, IFI/Plenum, New York.
- [31] Hayes, M., Masoomi, F., Schimmels, P., Randhir, K., Klausner, J., and Petrasch, J., 2021, "Ultra-High Temperature Thermal Conductivity Measurements of a Reactive Magnesium Manganese Oxide Porous Bed Using a Transient Hot Wire Method," *ASME J. Heat Transfer-Trans. ASME*, **143**(10), p. 104502.
- [32] Ziegler, J. G., and Nichols, N. B., 1993, "Optimum Settings for Automatic Controllers," *ASME J. Dyn. Syst. Meas. Control*, **115**(2B), pp. 220–222.
- [33] García, J., Chean Soo Too, Y., Vasquez Padilla, R., Beath, A., Kim, J.-S., and Sanjuan, M. E., 2018, "Multivariable Closed Control Loop Methodology for Heliostat Aiming Manipulation in Solar Central Receiver Systems," *ASME J. Sol. Energy Eng.*, **140**(3), p. 031010.
- [34] Kumar, N., and Sharma, A., 2022, "Design and Analysis of Nonlinear Controller for a Standalone Photovoltaic System Using Lyapunov Stability Theory," *ASME J. Sol. Energy Eng.*, **144**(1), p. 011003.